Incommensurate helimagnetic structure of Ba(Fe₁₋ₓScₓ)₁₂O₁₉ determined by single-crystal neutron diffraction

Seiya Tanaka,[1] Ryoji Kiyanagi ⓘ,[2] Yoshihisa Ishikawa ⓘ,[3] Yasushi Amako ⓘ,[4] Taku Iiyama ⓘ,[4] Ryusuke Futamura ⓘ,[4] Kenichi Maruyama,[1] and Shigenori Utsumi ⓘ[1,*]

[1]*Suwa University of Science, Chino, Nagano 391-0292, Japan*
[2]*J-PARC Center, Japan Atomic Energy Agency, Tokai, Ibaraki 319-1195, Japan*
[3]*Neutron Science and Technology Center, Comprehensive Research Organization for Science and Society, Tokai, Ibaraki 319-1106, Japan*
[4]*Faculty of Science, Shinshu University, Matsumoto, Nagano 390-8621, Japan*

Sc-substituted hexagonal ferrite Ba(Fe₁₋ₓScₓ)₁₂O₁₉ has an incommensurate helimagnetic structure. However, the incommensurate helimagnetic structure has not been sufficiently determined, and the mechanism via which the helimagnetism develops has not been studied. Time-of-flight-Laue single-crystal neutron diffraction measurements were performed at 4–6 K on single-crystal samples of Ba(Fe₁₋ₓScₓ)₁₂O₁₉ having Sc concentrations of $x = 0$, 0.128, 0.153, and 0.193. The incommensurate helimagnetic structure was determined by analyzing the magnitude and direction of the Fe^{3+} magnetic moments at the five Fe1–Fe5 sites ($2a$, $4e$, $4f_1$, $4f_2$, and $12k$). The development mechanism of the helimagnetic structure was discussed from the standpoint of superexchange interaction. The crystal structure analyses revealed that the Sc substitution enabled two significant events, namely, the coordination changes of Fe^{3+} and Sc^{3+} at the Fe2($4e$) site, resulting in the shortened bond distances of Fe2-O1 and the preferred substitution of Fe^{3+} at the Fe4($4f_2$) site with Sc^{3+}. The magnetic structure analyses revealed that the helimagnetic structure of Ba(Fe₁₋ₓScₓ)₁₂O₁₉ is a cone type whose base is in the ab plane and height is in the c-axis direction. The magnetic moments of Fe2($4e$), Fe4($4f_2$), and Fe5($12k$) are aligned with distinct angles, leading to the helimagnetic structure of Ba(Fe₁₋ₓScₓ)₁₂O₁₉, and can be explained by assuming that there is an antiferromagnetic superexchange interaction J_5 between Fe2($4e$) and Fe5($12k$) that is negligible in the $x = 0$ crystal. The shorter bond distance of Fe2-O1 in Sc-rich crystals revealed by the crystal structure analyses enhances the superexchange interaction J_5. However, the Sc^{3+} preference for Fe4($4f_2$) weakens J_3 and J_4. The relatively strong J_5 leads to competition among the three superexchange interactions, J_3, J_4, and J_5, resulting in the development of the helimagnetic structure. These findings facilitate the understanding of the essentials of the basic magnetic material BaFe₁₂O₁₉.

I. INTRODUCTION

M-type hexagonal ferrite expressed by the chemical formula AFe₁₂O₁₉ (A = Ba, Sr, Pb, etc.) is widely used as a general magnetic material in various industrial fields because of its high electrical resistance, magnetic anisotropy, Curie temperature, and excellent chemical stability [1]. The high magnetic permeability indicates its potential to be used as an electromagnetic wave absorbing material for fifth-generation (5G) mobile communication systems. Ba-containing BaFe₁₂O₁₉ is the most inexpensive and easily synthesized of the ferrites and hence is used as a permanent magnet in DC motors and magnetic recording media. It is being actively researched as a material that is indispensable to the maintenance of our current living standards and to the building of a sustainable society in the future. Figure 1(a) shows the crystal structure of BaFe₁₂O₁₉ in a unit cell, belonging to the space group $P6_3/mmc$ (No. 194) [2,3]. Ba^{2+}

and O^{2-} with large ionic radii form a close-packed structure along the c axis, and Fe^{3+} is coordinated in five sites surrounded by octahedral ($2a$, $4f_2$, $12k$), tetrahedral ($4f_1$), and bipyramidal ($4e$) O^{2-}. Each Fe site is labeled as Fe1 for $2a$, Fe2 for $4e$, Fe3 for $4f_1$, Fe4 for $4f_2$, and Fe5 for $12k$, according to past research. The Fe^{3+} at the $4e$ site is distributed into two equivalent $4e$ coordinates on either side of the mirror plane at $z = \frac{1}{4}$ [4]. BaFe₁₂O₁₉ assumes a ferrimagnetic structure collinear to the c axis over the entire temperature range below the Curie point ($T_C = 740$ K) [Fig. 1(a)]. The orientation of the Fe^{3+} magnetic moments is parallel to the c axis in Fe1($2a$), Fe2($4e$), and Fe5($12k$), and antiparallel in Fe3($4f_1$) and Fe4($4f_2$). Table S1 in the Supplemental Material [5] summarizes the type and number of ions in the unit cell and the coordination and direction of the Fe^{3+} magnetic moment in BaFe₁₂O₁₉. The ferrimagnetic structure of BaFe₁₂O₁₉ is described using Gorter's model of the four antiferromagnetic superexchange interaction paths J_1–J_4, that is, J_1 : Fe1-O4-Fe3, J_2 : Fe3-O4-Fe5, J_3 : Fe4-O5-Fe5, and J_4 : Fe2-O3-Fe4 [Fig. 1(b)] [6], where J_1–J_4 represent superexchange interactions. Figure 1(b) also shows that there
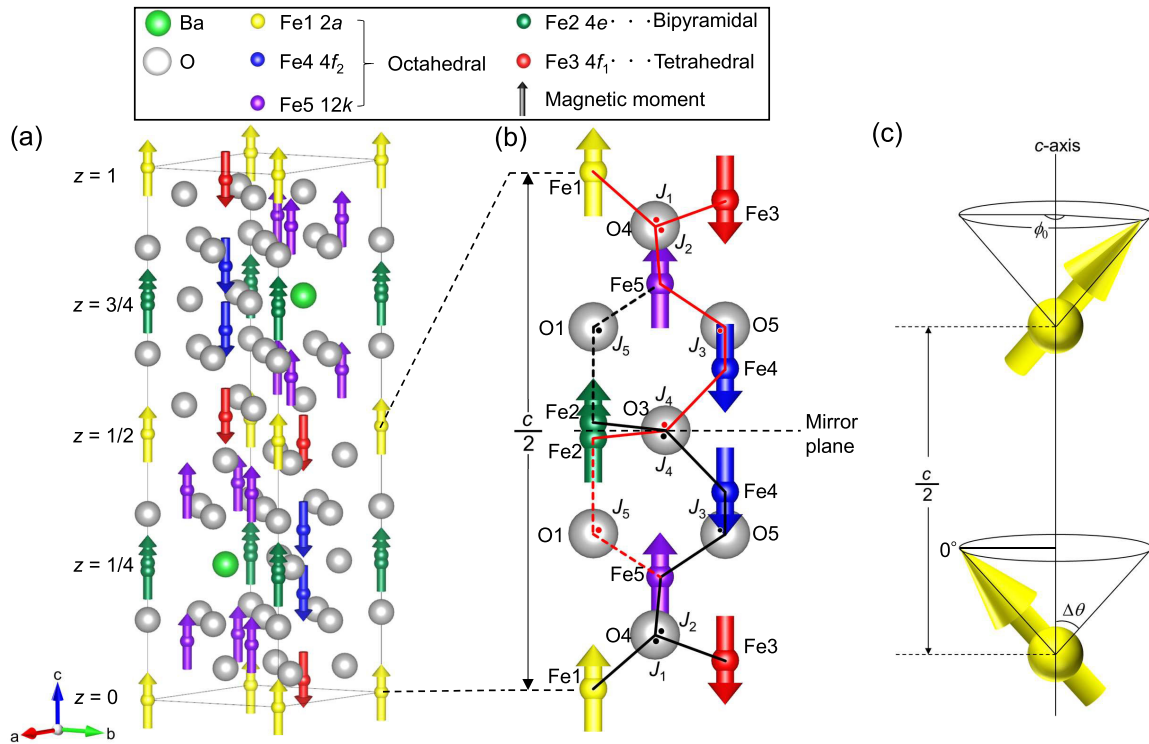

FIG. 1. (a) Crystal and ferrimagnetic structures of $BaFe_{12}O_{19}$ ($x = 0$) in unit cell. (b) Paths of four superexchange interactions J_1–J_4, indicated by two connected lines with a dot, for the ferrimagnetic case. Black and red lines indicate two possible cases, depending on the position of Fe2. The superexchange interaction J_5, which is assumed in this paper, is represented by two dashed lines with a dot for better understanding, though it is negligible in the ferrimagnetic structure. (c) Possible model of effective helimagnetic moments appearing in $Ba(Fe_{1-x}Sc_x)_{12}O_{19}$ ($x \gtrsim 0.06$). Each magnetic moment rotates by turn angle ϕ_0 of a helix in a $c/2$ cycle.

are two ferrimagnetic possibilities for the paths of the superexchange interactions, depending on the position of Fe2(4e), as indicated by the black and red lines.

Substituted M-type hexagonal ferrites have been studied extensively, as properties in dielectricity and magnetic permeability can be established upon substitution. The electromagnetic wave absorption properties of the Sn-substituted ferrite have been reported; this ferrite can absorb >99% of the incoming electromagnetic radiation in the frequency range 2–4 GHz [7]. An increase in the coercivity up to 11% with Nd-Co substitution has been reported [8]. Magnetic field-induced electrical polarization of $0.3\,\mu C/m^2$ has been detected at the liquid helium temperature with Ti-Co substitution [9].

Sc substitution has also been reported to instill properties in the material. For example, the Sc-substituted M-type hexagonal ferrite exhibits multiferroic properties in which electric polarization is induced by applying a transverse magnetic field [10]. The polycrystalline sample exhibits ferroelectricity even at zero magnetic field [11]. Thus, many studies have been performed aiming at practical applications such as low-energy consumption memory [12,13]. The previous studies imply that the conical spin structure appearing in $Ba(Fe_{1-x}Sc_x)_{12}O_{19}$, which is one type of helimagnetic structure, is vital for the multiferroic properties [10,14–18], where x is the concentration of Sc. The helimagnetism of $Ba(Fe_{1-x}Sc_x)_{12}O_{19}$ was initially studied in the 1960s; magnetization and magnetic anisotropy measurements showed that the magnetic moments in $Ba(Fe_{1-x}Sc_x)_{12}O_{19}$ have components in the direction of the

ab plane [19]. Magnetic satellite reflections were observed in the neutron diffraction pattern, confirming its helimagnetism [20].

Although the importance of the helimagnetism of $Ba(Fe_{1-x}Sc_x)_{12}O_{19}$ is known from the viewpoint of application, the details of the incommensurate helimagnetic structure of $Ba(Fe_{1-x}Sc_x)_{12}O_{19}$ have not been determined, and the mechanism by which the helimagnetism develops has not been sufficiently studied yet. One of the reasons for these issues is the difficulty in obtaining single crystals with high Sc concentrations x that exhibit the helimagnetism. Moreover, analyzing the helimagnetic structure in detail with polycrystalline samples is difficult because there are as many as five Fe sites. Although recent advances in science and technology have reduced the difficulties associated with collecting and analyzing neutron diffraction images, good quality single crystals are still necessary to establish the detailed incommensurate helimagnetic structures. In addition, to discuss the development mechanism of the helimagnetism, the investigation must be done from the standpoint of the superexchange interaction.

The superexchange interaction energy E_{ij}^{ex} is expressed by the following equation:

$$E_{ij}^{ex} = -2J\mathbf{S}_i \cdot \mathbf{S}_j, \tag{1}$$

where i and j are the number for the Fe1–Fe5 sites ($i \neq j$), $J(<0)$ is an exchange integral, and **S** is the Fe^{3+} magnetic moment. From Eq. (1), apparently, the Sc occupancy in the

Fe site, the magnitude and direction of the Fe^{3+} magnetic moments, and the steric configuration of the ions in terms of the exchange integral J are involved in developing the helimagnetism. All these factors may be derived from the neutron diffraction data.

We have previously succeeded in synthesizing single crystals of $Ba(Fe_{1-x}Sc_x)_{12}O_{19}$ with various Sc concentrations x using the flux method [21]. Single-crystal neutron diffraction measurements were performed on the grown single crystals to construct the magnetic phase diagram with respect to Sc concentration (x) and temperature (T). The incommensurate helimagnetic moment appearing at $x \gtrsim 0.06$ is canted by $\Delta\theta$ against the c axis [Fig. 1(c)] and rotates by the turn angle ϕ_0 of the helix in the $c/2$ cycle. Here, ϕ_0 is calculated by the relationship $\phi_0 = 2\pi k$ using the magnetic propagation vector **k** $(00\,k)$ $(0 < k \leqslant 0.5)$. Further addition of Sc^{3+} induces a spin-canted magnetic structure with $\Delta\theta \neq 90°$ and $\phi_0 = 180°$ $(k = 0.5)$ at $x \gtrsim 0.19$ [22].

In our previous work [22], we performed single-crystal neutron diffraction measurements for the determination of the magnetic phases. However, the data collected in these experiments were inadequate for the detailed incommensurate helimagnetic structure analysis since the diffraction peaks were observed from only one crystal orientation and the measurements were performed within a short period of time. In this paper, we perform time-of-flight (TOF)-Laue single-crystal neutron diffraction measurements at 4–6 K on single-crystal samples of $Ba(Fe_{1-x}Sc_x)_{12}O_{19}$ with $x = 0$, 0.128, 0.153, and 0.193 to determine the details of their incommensurate helimagnetic structures and clarify the development mechanism of the helimagnetism. The crystal structure analyses were performed to determine the coordinates of each ion and Sc site occupancy, which are directly linked to the superexchange interaction energy. The magnetic structure analyses were performed to determine the detailed incommensurate helimagnetic and spin-canted magnetic structures, that is, the magnitude and direction of the Fe^{3+} magnetic moment at each Fe site. Subsequently, in this paper, the magnetic structures are discussed from the viewpoint of the superexchange interaction to reveal the development mechanism of the helimagnetism in $Ba(Fe_{1-x}Sc_x)_{12}O_{19}$. The results of this paper should enhance our understanding of the magnetism in hexagonal ferrites and be useful in the design of magnetic oxide materials.

II. METHODS

Single-crystal samples of $Ba(Fe_{1-x}Sc_x)_{12}O_{19}$ grown by the flux method were used. Details regarding the growth of the single crystals can be found in our previous paper [21]. A brief explanation follows: The spontaneous crystallization from the subsystem $BaO\text{-}Fe_2O_3\text{-}Sc_2O_3\text{-}Na_2O$ was employed. Powdered $BaCO_3$ (Wako Pure Chemical Co.), Fe_2O_3 (Kanto Chemical Co., Inc.), Sc_2O_3 (Shin-Etsu Chemical Co., Ltd.), and Na_2CO_3 (Wako Pure Chemical Co.) were used as starting reagents, where Na_2O and a portion of Fe_2O_3 work as a flux. $BaCO_3$, Fe_2O_3, and Na_2CO_3 were special-grade chemicals. The reagents were weighed in an accuracy of 1 mg, packed in an uncovered platinum crucible, and heated to 1693 K for 20 h using an electric furnace. After confirming crystal nucleation by *in situ* observation during slow cooling, crystals were grown at a slow cooling rate of 0.5 K/h. The crystals were obtained after washing away the flux with hot dilute nitric acid. The obtained crystals were examined using x-ray diffraction (Rigaku: MiniFlexII) of CuK_α radiation to determine the crystal phase. The chemical composition and Sc concentration x of the obtained crystals were determined by elemental analysis using energy dispersive x-ray spectroscopy [JEOL: JSD-2300(S)].

Single-crystal neutron diffraction measurements were performed with a TOF-Laue single-crystal neutron diffractometer, SENJU, installed at BL18 of the Materials and Life Science Experimental Facility (MLF) in J-PARC (Japan) [23]. The wavelength range of incident neutrons was 0.4 to 4.4 Å. The crystal size was $5 \times 3 \times 2$ mm^3 (0.16 g) for $x = 0$, $4 \times 3 \times 2$ mm^3 (0.12 g) for $x = 0.128$, $3 \times 2 \times 1$ mm^3 (0.03 g) for $x = 0.153$, and $2 \times 2 \times 1$ mm^3 (0.02 g) for $x = 0.193$. The measurement temperature was 4 K for $x = 0$, 0.128, 0.153, and 6 K for $x = 0.193$. The data reduction and the determination of the UB matrix were performed using the data processing software STARGazer [24]. The crystal and magnetic structures were refined using the software JANA2006 and JANA2020 [25].

The magnetization curves of the single-crystal samples were measured at 2 K using a superconducting quantum interference device (SQUID) magnetometer (Quantum Design, MPMS3). The external magnetic field of strength up to 70 kOe was applied to the directions of the c axis and the ab plane. VESTA is used for the visualization of crystal and magnetic structures [26].

III. RESULTS AND DISCUSSION

A. Neutron diffraction experiments and refinement

The experimental and refinement parameters of the neutron diffraction measurements are listed in Table I. The lattice constants a and c increase with x due to the substitution of Sc^{3+} which has a larger ionic radius than Fe^{3+}. Figure 2 shows the $(00l)$ neutron diffraction patterns for $x = 0$, 0.128, 0.153, and 0.193 at $T = 4$–6 K. Diffraction peaks for the $x = 0$ crystal appear only at $(00\,2n)$ due to the $P6_3/mmc$ symmetry, where n is an integer. Incommensurate magnetic satellite reflections appear at $[00\,2(n \pm k)]$ for $x = 0.128$ and 0.153, indicating the development of the helimagnetic structure, here, $k = 0.399$ for $x = 0.128$ and $k = 0.493$ for $x = 0.153$, respectively. Commensurate magnetic reflections appear at $[00\,2(n \pm 0.5)]$ for $x = 0.193$, indicating the development of the spin-canted magnetic structure. The R and wR factors shown in Table I, which indicate the reliability of the analysis, are 7.16–10.13 for the main reflections including nuclear and magnetic scattering corresponding to the magnetic structure components that obey the $P6_3/mmc$ symmetry and 12.00–14.23 for the satellite reflections including pure magnetic scattering corresponding to the helimagnetic and the spin-canted magnetic structures components. The representative comparison of the observed and calculated values of the crystal and magnetic structure factors, F_{obs} and F_{cal}, for the $x = 0.153$ crystal is shown in Fig. S1 in the Supplemental Material [5].

TABLE I. Experimental and refinement parameters of neutron diffraction.

Sc concentration x	0	0.128	0.153	0.193
Chemical formula	$BaFe_{12}O_{19}$	$BaFe_{10.464}Sc_{1.536}O_{19}$	$BaFe_{10.164}Sc_{1.836}O_{19}$	$BaFe_{9.684}Sc_{2.316}O_{19}$
Crystal system			Hexagonal	
Space group			$P6_3/mmc$ (No. 194)	
Magnetic space group	$P6_3/mm'c'$		$P2_1(00\gamma)0$	$P2_1$
a(Å)	5.8878(4)	5.9186(8)	5.9382(8)	5.9447(3)
c(Å)	23.097(2)	23.539(6)	23.618(4)	23.652(2)
Density (g/cm^{-3})	5.324	5.091	5.026	4.984
Magnetic propagation vector **k**	(0 0 0)	(0 0 0.399(1))	(0 0 0.439(1))	(0 0 0.5)
No. of observed main reflections ($I > 3\sigma$)	1320	1336	2394	3781
No. of observed satellites ($I > 3\sigma$)	–	96	92	82
R (main reflections)	5.60	7.18	4.91	6.63
wR (main reflections)	8.09	9.97	7.16	10.13
R (satellites)	–	9.87	8.04	12.31
wR (satellites)	–	14.23	12.00	14.09

B. Crystal structure changes by Sc substitution

We analyzed the crystal structures of each single-crystal sample at low temperatures to clarify the structure change due to the Sc substitution, especially the steric configuration of the bipyramid, tetrahedron, and octahedron containing Fe/Sc ions. The crystal structure analyses were performed under the assumption that the site occupancies of Ba, O, and (Fe + Sc) are 1.0 and the equivalent isotropic temperature parameters U_{eq} of Fe^{3+} and Sc^{3+} at the same site are equal. The crystal system maintained $P6_3/mmc$ without any phase transition despite the Sc substitution, which agrees with the results obtained from powder neutron diffraction measurements [11]. The atomic fractional coordinates U_{eq} and site occupancies of each ion obtained with various x crystals can be seen in Table S2 in the Supplemental Material [5]. The crystal

structure analyses of each of the single crystals provides information on changes in the Sc^{3+} occupancy in each Fe site; they also provide the steric configuration of superexchange interactions, bond distances, and angles Θ_J of the superexchange interactions, which could affect the development of the helimagnetism.

Figure 3 shows the Sc occupancy at each Fe site as a function of x. The Sc occupancy at every Fe site increases linearly with increasing x. The black dotted line in Fig. 3 indicates an imaginary Sc occupancy when Sc is uniformly distributed over the five Fe sites. It is found that Sc^{3+} preferentially substitutes Fe^{3+} at the Fe4($4f_2$) site in the measured range of $x \leqslant 0.2$ because the Sc occupancy in the Fe4 site is clearly above the uniformity line. This result agrees with those obtained from the *ab initio* calculations [27].
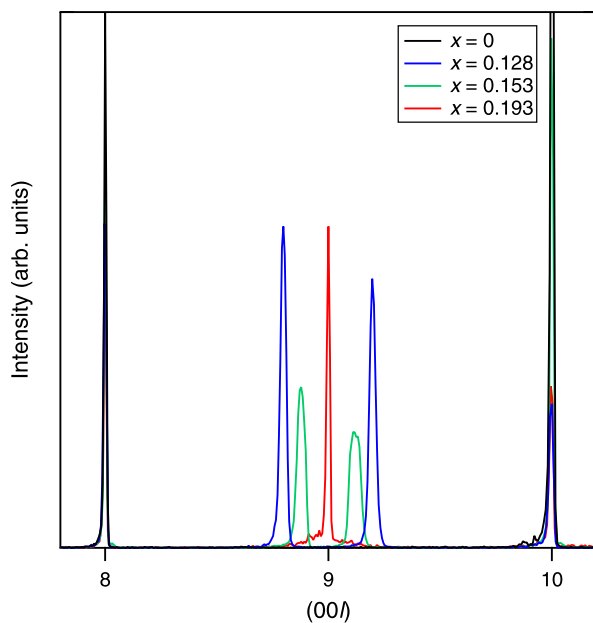

FIG. 2. (00l) neutron diffraction patterns whose abscissa is expressed by l for the $x = 0$, 0.128, 0.153, and 0.193 crystals at $T = 4$–6 K.
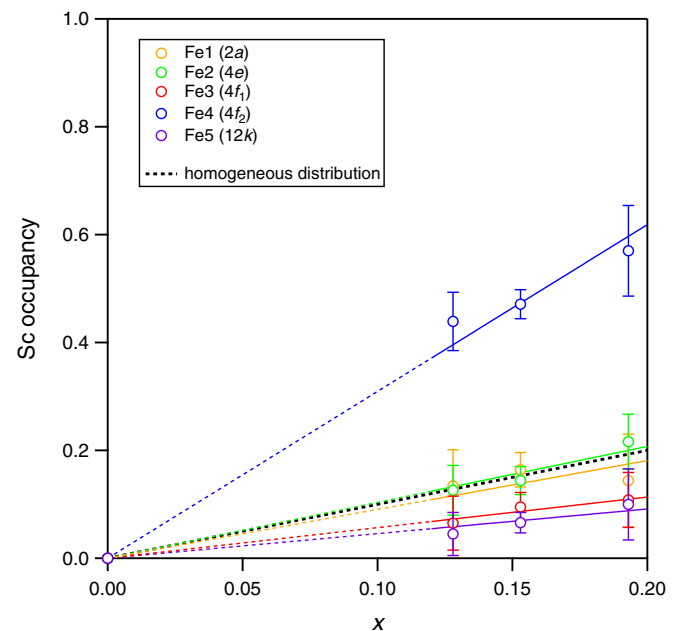

FIG. 3. Sc occupancy at each Fe site as a function of x. The dotted black line shows occupancy when Sc is homogeneously distributed over five sites.
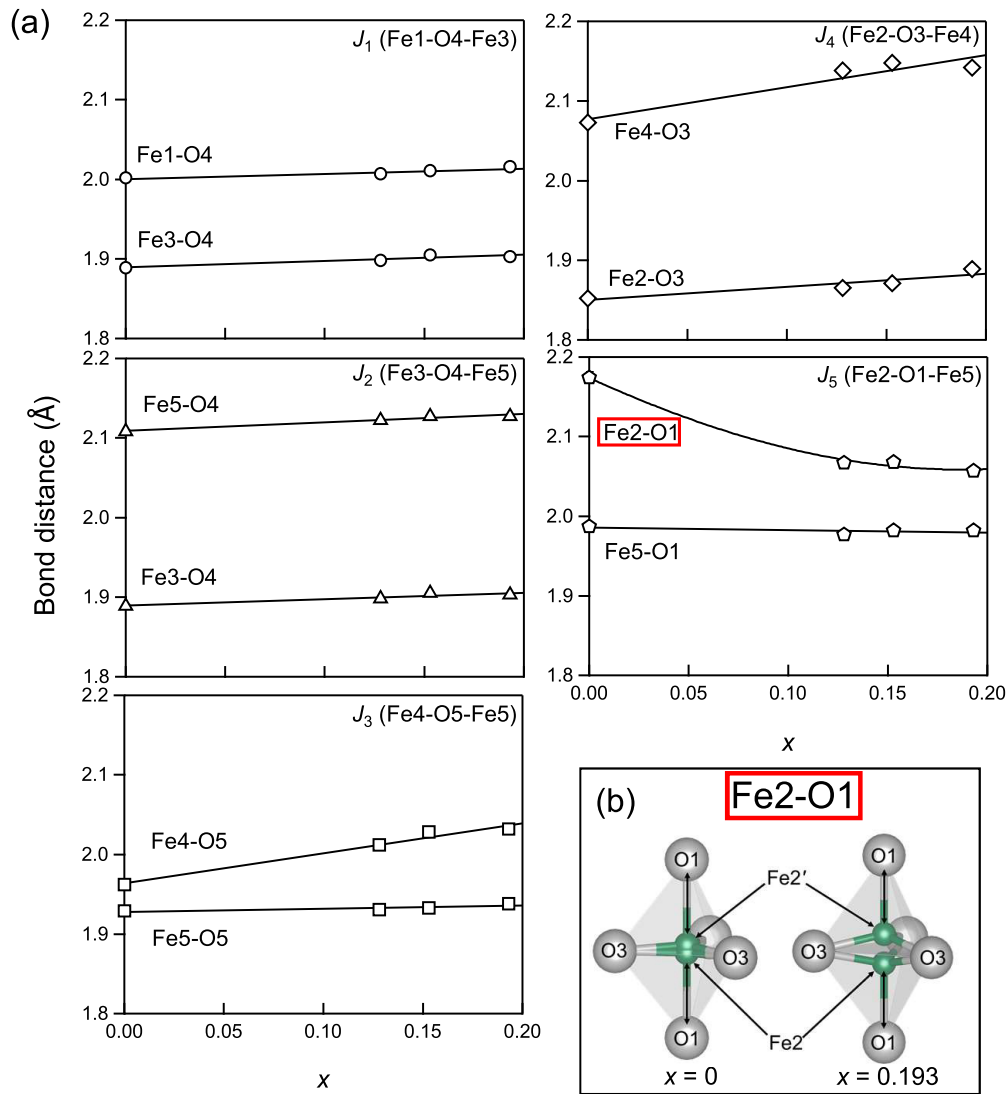
FIG. 4. (a) Bond distances, Fe-O, of superexchange interactions J_1–J_5 as a function of x. (b) Steric configuration of Fe2-O1 associated with J_5 (Fe2-O1-Fe5) for $x = 0$ and 0.193. Standard deviations are contained within markers.

Figure 4(a) shows the Fe-O bond distances as a function of x of four known superexchange interactions J_1–J_4 described in Fig. 1(b) and of a superexchange interaction J_5 described in detail in Sec. III D. The bond distances shown in Fig. 4(a) for J_1–J_4 tend to increase with increasing x, which is a normal change because the lattice expands when Fe^{3+} is substituted by Sc^{3+} which has a larger ionic radius than Fe^{3+}. The bond distances Fe4-O3 and Fe4-O5, associated with the Fe4 site, which were previously shown to be preferentially substituted by Sc^{3+}, increase slightly more than those of the other bonds. The expanding bond distances of Fe4-O3 and Fe4-O5 suggest that the superexchange interactions of J_3 and J_4 are weakened by Sc substitution. Special attention should be paid to the bond distance Fe2-O1, which decreases significantly with increasing x. This is due to the remarkable position change of Fe2 upon Sc substitution [Fig. 4(b)]. Fe2 comprises two split unstable sites with a double-well potential with respect to the mirror plane at $z = \frac{1}{4}$ (and $\frac{3}{4}$) [28]. The substitution of Sc^{3+}, with a large ionic radius, causes more fluctuations and widens the distance between

the two Fe2 sites. The Fe2-Fe2′ distance increases significantly from 0.2 Å at $x = 0$ to 0.8 Å at $x = 0.193$. Thus, the remaining Fe2-O1 distance is notably reduced, suggesting that the superexchange interaction of J_5 is strengthened by Sc substitution.

Figure 5 shows the included angles Θ_{J1}–Θ_{J5} of the superexchange interactions J_1–J_5 as a function of x. Here, Θ_{J4} and Θ'_{J4} are used to represent the two paths of the superexchange interaction Fe2-O3-Fe4 caused by the split of the Fe2 positions. While the changes of Θ_{J1}, Θ_{J2}, Θ_{J3}, and Θ_{J5} are negligible, Θ_{J4} and Θ'_{J4} change notably due to the increased splitting of the Fe2 sites, that is, as x increases, Θ_{J4} increases and Θ'_{J4} decreases markedly.

C. Incommensurate helimagnetic structure of Ba(Fe$_{1-x}$Sc$_x$)$_{12}$O$_{19}$

To perform the detailed magnetic structure analyses, the magnetic moment of each Fe(j) site is expressed by the magnitude m_{j_ab} in the ab plane, the rotation angle φ_j in
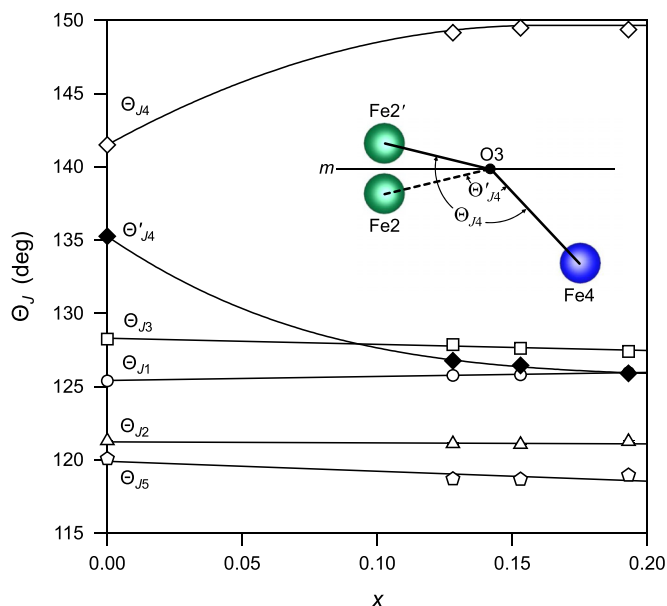
FIG. 5. Included angles, Θ_{J1}–Θ_{J5}, of superexchange interactions J_1–J_5 as a function of x. Standard deviations are contained within markers.

the ab plane, and the z-axis component m_{j_z} of the magnetic moments along the c axis using the cylindrical coordinate system as shown in Fig. S2(a) in the Supplemental Material [5]. This cylindrical representation helps to reduce the number of unknown parameters that must be determined from the magnetic satellite reflections since m_{j_z} can be determined independently from the main reflections. Here, φ_j of the Fe1 site at $z = 0$ is set as the origin ($0°$) of φ_j in the ab plane. A detailed description on the cylindrical coordinates used for the analyses is provided in the Supplemental Material [5]. While the crystal structure of $\mathrm{Ba(Fe_{1-x}Sc_x)_{12}O_{19}}$ maintains the space group $P6_3/mmc$, the space group of its magnetic structure should be changed, as can be seen from the appearance of the incommensurate magnetic satellite reflections in the neutron diffraction pattern in Fig. 2. The magnetic structure analyses revealed that the magnetic space group and magnetic super space group were well refined by $P6_3/mm'c'$ for the ferrimagnetic phase ($x = 0$), by $P2_1(00\gamma)0$ for the helimagnetic phase ($x = 0.128$ and 0.153), and by $P2_1$ for the spin-canted magnetic phase ($x = 0.193$) (see Table I). Here, γ represents the possibility of having a magnetic propagation vector in the l direction. The detailed determination process of the magnetic space groups for magnetic structures in $\mathrm{Ba(Fe_{1-x}Sc_x)_{12}O_{19}}$ is described in the Supplemental Material [5,22,29]. Considering the symmetry of the crystal structure of $P6_3/mmc$, the magnetic moments at the five Fe sites from $z = 0$ to $\frac{1}{4}$ were determined for the ferrimagnetic case of the $x = 0$ crystal. For the helimagnetic and spin-canted magnetic cases, the magnetic moments of 10 Fe sites from $z = 0$ to $\frac{1}{2}$ were determined because the crystal symmetry of $P6_3/mmc$ is broken. Considering the crystal symmetry of $z = 0$ to $\frac{1}{4}$ and $\frac{1}{4}$ to $\frac{1}{2}$, the rotation angle φ'_j from $z = \frac{1}{4}$ to $\frac{1}{2}$ can be expressed as follows:

$$\varphi'_j = \phi_0 - \varphi_j, \quad (2)$$

using the rotation angle φ_j from $z = 0$ to $\frac{1}{4}$. The turn angle ϕ_0 of the helix rotates in the ab plane for the site-equivalent magnetic moments in the range $z = \frac{1}{2}$ to 1. As the symmetry of $P2_1$ also maintains the symmetry along the c axis, the component m'_{j_z} of the magnetic moments along the c axis for $z = \frac{1}{4}$ to $\frac{1}{2}$ is

$$m'_{j\_z} = m_{j\_z}. \quad (3)$$

Similarly, the component m'_{j_ab} of the magnetic moments in the ab plane for $z = \frac{1}{4}$ to $\frac{1}{2}$ is

$$m'_{j\_ab} = m_{j\_ab}. \quad (4)$$

Equations (3) and (4) yield the following Eq. (5) for the canting angle $\Delta\theta'_j$ for $z = \frac{1}{4}$ to $\frac{1}{2}$ in the polar coordinate system, which will be discussed later:

$$\Delta\theta'_j = \Delta\theta_j. \quad (5)$$

Here, we assume that the magnetic moments of the same Fe site at the same c-axis coordinate are of the same magnitude and are arranged ferromagnetically.

However, polar coordinates, the magnitude m_j, the rotation angle φ_j in the ab plane, and the canting angle $\Delta\theta_j$ from the ferrimagnetic case θ_j (Fig. 1(c) and Table S1 in the Supplemental Material [5]) ($\theta_j = 0°$ or $180°$), as shown in Fig. S2(b) in the Supplemental Material [5], are used to draw the helimagnetic and the spin-canted magnetic structures in this paper. This is because they provide a visual comprehension of the helimagnetic and spin-canted magnetic structures and an easy understanding of the canting angle $\Delta\theta_j$ from the ferrimagnetic structure. The magnitude of the magnetic moment m_j, the canting angle $\Delta\theta_j$, and the rotation angle φ_j of each Fe(j) site determined for various crystals with different x values are shown in Table II. The magnetic structure obtained for the $x = 0$ crystal supports the Gorter's ferrimagnetic model shown in Fig. 1(a), and the magnitude of the Fe^{3+} magnetic moments at 4 K are close to the theoretical value of 5 μ_B at 0 K. However, the magnetic moments for the $x = 0.128$, 0.153, and 0.193 crystals were noticeably $<5 \mu_B$, which is like the values reported for polycrystalline samples [11] and analogous materials [30]. The shrinkage of the magnetic moment is presumably attributed to the spin-glass-like behavior [11]. The spin-glass-like behavior can also be observed in the magnetization curves of each x in terms of Bohr magnetons n_B per formula unit at 2 K (Fig. 6) when the external magnetic field was applied to the c axis and ab plane. The magnetization n_B of the $x = 0$ crystal is nearly saturated to the theoretical value of 20 μ_B at 5 kOe in the direction of the c axis and 18 kOe in the ab plane and remains constant thereafter. In contrast, n_B values of the crystals with $x = 0.128$, 0.153, and 0.193 increase rapidly to 10 kOe in both the c-axis or ab-plane directions and thereafter gradually increase to 70 kOe. This gradual increase in n_B may be the process by which the random magnetic moments of the spin-glass-like state align with the direction of the magnetic field. Note that no direct evidence for the spin-glass-like state, such as magnetic diffuse scattering, was observed in our measurement, and the spin-glass-like state is to be further investigated.

Based on the orientation of the magnetic moments obtained from the analysis, the three-dimensional model of the

TABLE II. Results of magnetic structure refinements. Magnitude of magnetic moment m_j and canting angle $\Delta\theta_j$ from ferrimagnetic case and rotation angle φ_j and φ'_j from φ_1 as the origin for each x.

Site	$x = 0$	$x = 0.128$				$x = 0.153$				$x = 0.193$			
	m_j	m_j	$\Delta\theta_j$	φ_j	φ'_j	m_j	$\Delta\theta_j$	φ_j	φ'_j	m_j	$\Delta\theta_j$	φ_j	φ'_j
Fe(j)	(μ_B)	(μ_B)		(deg)		(μ_B)		(deg)		(μ_B)		(deg)	
Fe1	4.2(2)	5.2(2)	44(0)	0(−)	144(−)	4.1(1)	90(−)	0(−)	158(−)	4.3(1)	85(1)	0(−)	180(−)
Fe2	4.3(2)	3.0(4)	78(5)	133(2)	11(2)	3.1(5)	59(12)	167(2)	351(2)	3.0(3)	87(2)	199(11)	341(11)
Fe3	5.1(2)	3.6(2)	74(4)	181(1)	323(1)	3.7(1)	99(5)	179(1)	339(1)	4.1(1)	85(2)	176(3)	4(3)
Fe4	5.0(2)	3.7(3)	27(6)	185(5)	319(5)	3.7(5)	29(7)	197(2)	321(2)	3.3(3)	48(4)	252(7)	288(7)
Fe5	4.2(2)	3.0(1)	57(3)	3(1)	141(1)	2.8(2)	75(6)	359(1)	159(1)	2.5(1)	85(2)	345(4)	195(4)

incommensurate helimagnetic structure of the $x = 0.153$ crystal is illustrated in Fig. 7(a). The top views of the orientations of the magnetic moments in the range $0 \leqslant z < \frac{1}{2}$ projected onto the ab plane showing φ_j and the side views of the orientations of the magnetic moments in the range $0 \leqslant z \leqslant 1$ projected onto the bc plane along the a axis showing $\Delta\theta_j$ are shown in Figs. 7(b)–7(d) for the $x = 0.128, 0.153$, and 0.193 crystals. Although φ_j is shown only in the range from $z = 0$ to $\frac{1}{2}$, each magnetic moment at the same site in the range $z = \frac{1}{2}$

to 1 rotates by ϕ_0 in the ab plane, as their magnetic space groups are $P2_1$. Here, the arrows in Fig. 7, representing the magnetic moments, are drawn as the same size, regardless of their magnitude, to clearly depict the arrangement of the magnetic moments. As shown in Fig. 7(a), the helimagnetic structure of Ba(Fe$_{1-x}$Sc$_x$)$_{12}$O$_{19}$ is a cone type with the base in the ab plane and the height along the c axis; the proper screw structure in the ab plane propagates along the c-axis direction.
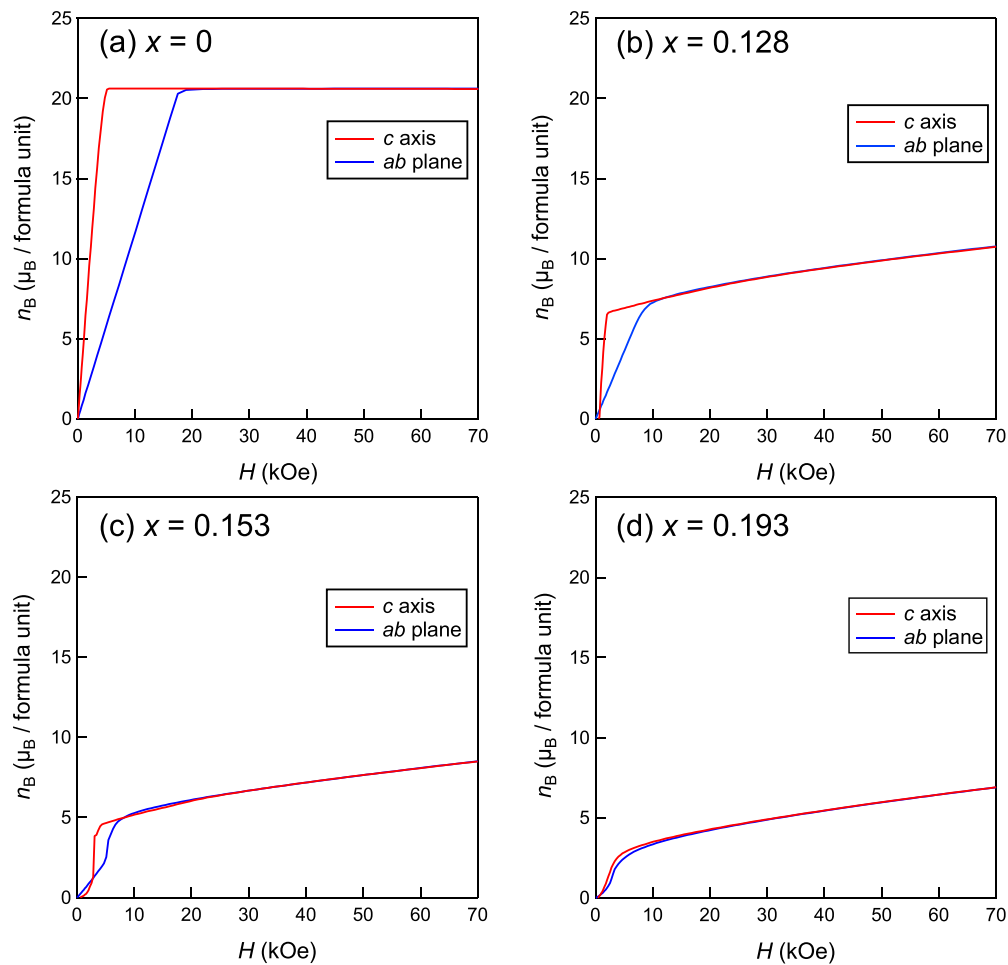

FIG. 6. Magnetization curves of (a) $x = 0$, (b) $x = 0.128$, (c) $x = 0.153$, and (d) $x = 0.193$ crystals measured at 2 K. Magnetization is expressed in Bohr magnetons n_B per formula unit. External magnetic field was applied along the c-axis (red line) and ab-plane (blue line) directions.
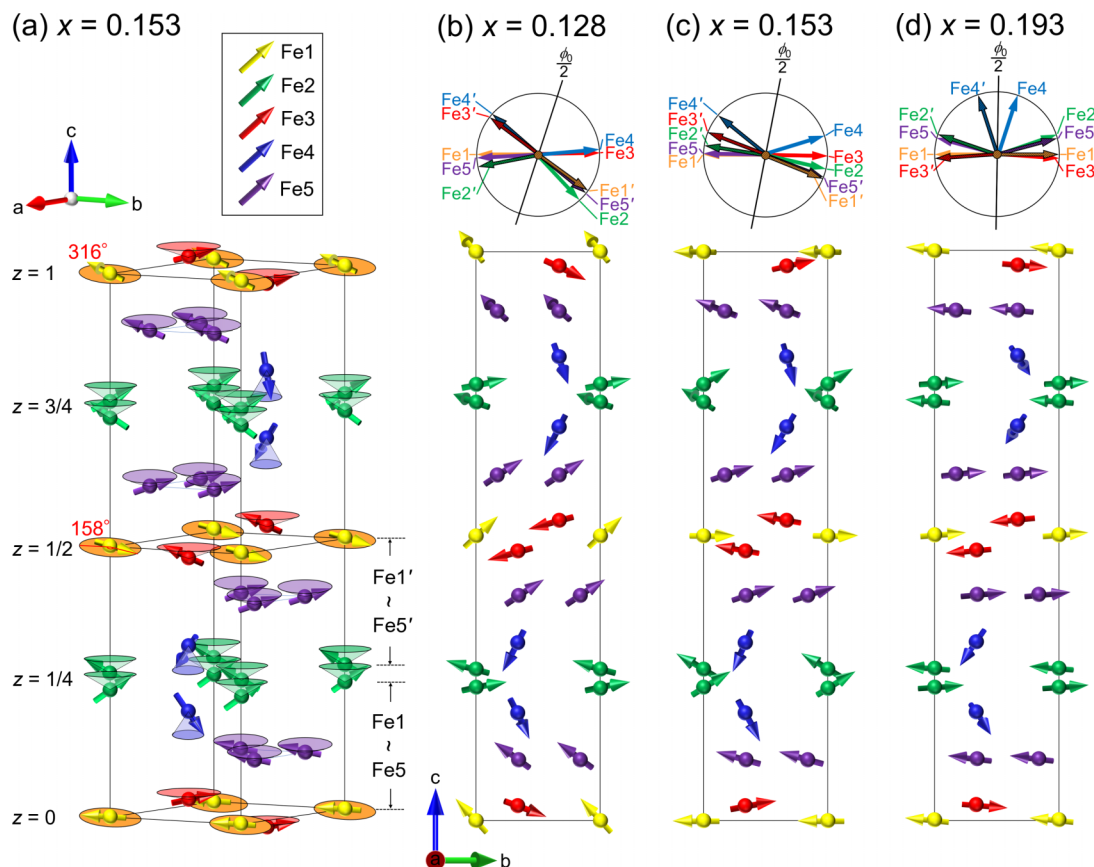
FIG. 7. (a) Incommensurate helimagnetic structure of $Ba(Fe_{1-x}Sc_x)_{12}O_{19}$ with $x = 0.153$. Arrows on the cones denote Fe1–Fe5 magnetic moments, respectively. (b)–(d) Representation of the magnetic structure models for $x = 0.128$, 0.153, and 0.193 crystals, projected along the a axis and top views with respect to Fe1 ($z = 0 - \frac{1}{2}$). Magnetic moments in the top views are represented darker for $0 \leqslant z < \frac{1}{4}$ and lighter with black edges for $\frac{1}{4} < z \leqslant \frac{1}{2}$.

The rotation angle φ_j in the ab plane appears to behave erratically as x increases. However, when considering the absolute value of the angle differences $|\Delta\varphi_j|$ between φ_j and φ_j' at the same Fe site, shown in Table III, $|\Delta\varphi_2|$ and $|\Delta\varphi_4|$ deviate from ϕ_0. The angle $\Delta\theta_j$ (Table II) of each magnetic moment and ϕ_0 tend to increase with increasing x. For the $x = 0.193$ crystal, $\Delta\theta_1$, $\Delta\theta_2$, $\Delta\theta_3$, and $\Delta\theta_5$ are $\sim 90°$, that is, the magnetic moments at the Fe1, Fe2, Fe3, and Fe5 sites almost lie in the ab plane, while that of Fe4 has a finite magnetic moment along the c axis. Because $|\Delta\varphi_4|$ is quite different from ϕ_0 and $\Delta\theta_4$ is significantly smaller than $90°$, the superexchange interactions with respect to the Fe4 site should

be deeply involved in the development of the helimagnetic structure.

D. Development mechanism of helimagnetic structure

We discuss the reason why Sc substitution induces the helimagnetic structure from the perspective of superexchange interactions. The ferrimagnetic structure of Sc-free $BaFe_{12}O_{19}$ is explained by four superexchange interactions J_1–J_4, as shown in Fig. 8(a). The results of the magnetic structure analysis clearly show that the absolute value of the angle difference $|\Delta\varphi_2|$ of Fe2 and the canting angle $\Delta\theta_4$ of Fe4 differ from the others with increasing x. This angular arrangement of Fe2 and Fe4 can be explained by assuming an antiferromagnetic superexchange interaction of J_5 (Fe2-O1-Fe5) between magnetic moments at Fe2 and Fe5. Figure 9 shows the angles α_J formed by the magnetic moments coupled by the four superexchange interactions J_1–J_4 and the J_5 interaction, which reflect the strength of the superexchange interactions; the closer to $180°$ α_J, the stronger the antiferromagnetic coupling. In the $x = 0$ crystal, α_J of J_1–J_4 is all antiferromagnetic coupling ($180°$), resulting in the collinear ferrimagnetic structure. However, α_{J5} in the $x = 0$ crystal is $0°$, indicating that J_5 is not in effect. Thus, the paths of the superexchange interactions are as shown in Fig. 8(a). As can be seen in Fig. 9, α_{J5} of J_5 increases from $\approx 90°$ ($x = 0.06$)

TABLE III. Absolute value of angle difference $|\Delta\varphi_j|$ between φ_j and φ_j' for each Fe site with $x = 0.128$, 0.153, 0.193. Turn angle ϕ_0 of the helix is shown for comparison.

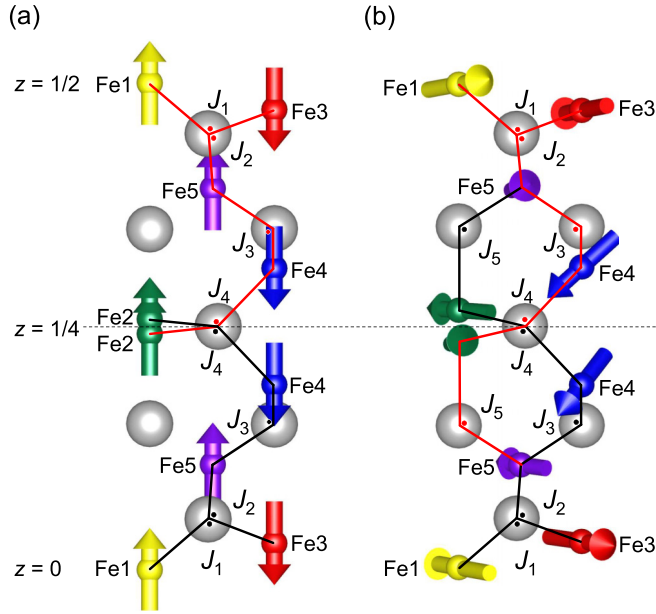| (deg)	$x = 0.128$	$x = 0.153$	$x = 0.193$
ϕ_0	144	158	180
$|\Delta\varphi_1|$	144(–)	158(–)	180(–)
$|\Delta\varphi_2|$	122(2)	176(2)	142(11)
$|\Delta\varphi_3|$	142(1)	160(1)	172(3)
$|\Delta\varphi_4|$	134(5)	124(2)	26(7)
$|\Delta\varphi_5|$	138(1)	160(1)	150(4)

FIG. 8. (a) Four superexchange interactions J_1–J_4 that describe the ferrimagnetic structure. (b) Five superexchange interactions in the helimagnetic and spin-canted magnetic structures of Ba(Fe$_{1-x}$Sc$_x$)$_{12}$O$_{19}$, assuming superexchange interaction J_5. There are three competing superexchange interactions, J_3, J_4, and J_5.

FIG. 9. Angles α_{J1}–α_{J5} formed by magnetic moments connected through superexchange interactions J_1–J_5 as a function of x.

to 134° ($x = 0.193$) with increasing x, while α_{J3} and α_{J4} decrease from 180° to 96° and from 180° to 91°, respectively. The increase in α_{J5} implies that the superexchange interaction J_5 is strengthened by Sc substitution and its antiferromagnetic coupling comes into effect. The decreases in α_{J3} and α_{J4} imply that the superexchange interactions J_3 and J_4 are weakened by Sc substitution. These facts induce competition among the three superexchange interactions J_3, J_4, and J_5 in the Sc-rich crystal. The paths of superexchange interactions in the Sc-rich crystals are shown in Fig. 8(b), which depicts three competing superexchange interactions. The three magnetic moments at the Fe2, Fe4, and Fe5 sites orient in different directions with distinct angles, developing the helimagnetic structure. The canting angle $\Delta\theta_4$ of Fe4 is small, probably because it acts as a buffer for Fe2 and Fe5 that lie in the ab-plane direction due to mutual antiferromagnetic coupling. The angles α_{J1} and α_{J2} of J_1 and J_2, which are noncompetitive superexchange interactions, almost maintain the antiferromagnetic couplings, though they slightly deviate from 180° due to the different magnetic anisotropies in the c-axis and ab-plane directions in the $x = 0.128$ and 0.153 crystals, as seen from Fig. 6. The $x = 0$ crystal exhibits a strong magnetic anisotropy, which is characteristic of BaFe$_{12}$O$_{19}$. The crystals with $x = 0.128$ and 0.153 also show magnetic anisotropy because the magnetization curves in the c-axis and ab-plane directions do not coincide in the low magnetic fields, although the crystal with $x = 0.193$ shows almost no anisotropy.

The strengthening of J_5 and the weakening of J_3 and J_4 due to the Sc substitution are supported by changes in the crystal structure. The Sc substitution significantly shortens the bond distance Fe2-O1 of the superexchange interaction J_5, as shown in Fig. 4(a). This strengthens J_5 due to the enhanced
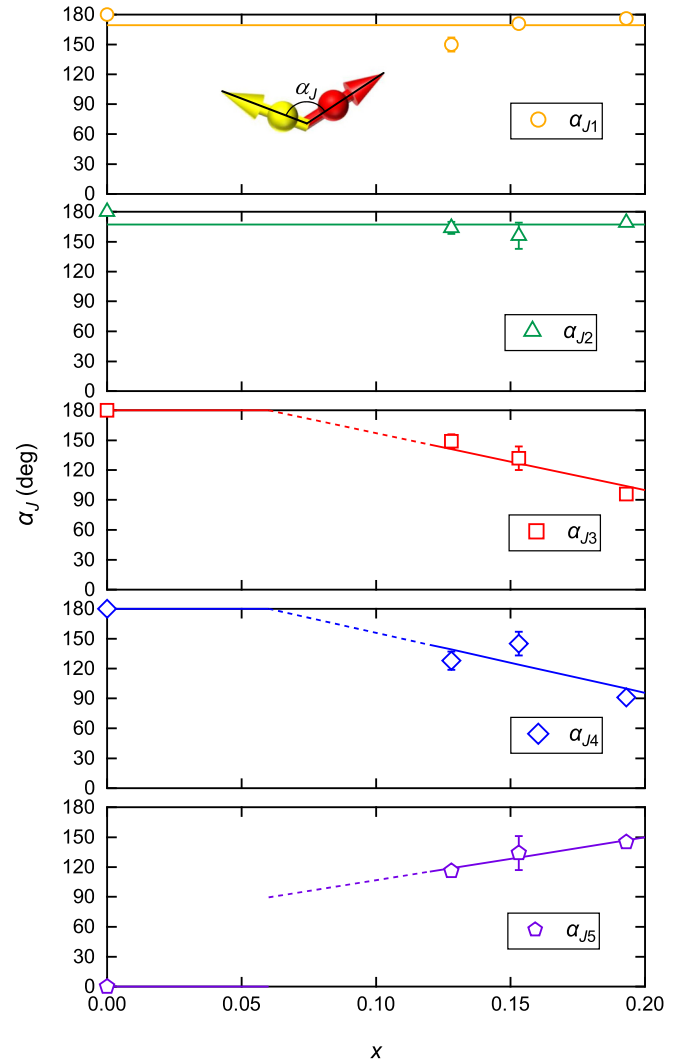
covalency between Fe2 and O1. However, Sc^{3+} preferentially substitutes for Fe4, as shown in Fig. 3, which weakens J_3 and J_4, as can be seen from Eq. (1). As a result, the strengths of the three competing superexchange interactions J_3, J_4, and J_5 become comparable and develop the helimagnetic structures of $x = 0.128$ and 0.153. A further increase in x enhances J_5 to be much stronger than J_3 and J_4 at $x = 0.193$. The magnetic moments at the Fe2 and Fe5 sites coupled through J_5 are antiparallel to develop the spin-canted magnetic structure. Note that, as described so far, the Fe2 ion plays an important role in developing the helimagnetic structure. The Fe2 ion is also involved in the ferroelectricity; thus, the multiferroicity observed in this material may be caused via the Fe2 ion.

IV. CONCLUSIONS

TOF-Laue single-crystal neutron diffraction measurements at 4–6 K were performed on single-crystal samples of Ba(Fe$_{1-x}$Sc$_x$)$_{12}$O$_{19}$ with Sc concentrations of $x = 0$, 0.128, 0.153, and 0.193. The crystal structure analyses revealed that the bond distance Fe2-O1 was shortened by Sc substitution,

and Sc^{3+} preferentially substituted Fe^{3+} at the Fe4 site. The magnetic structure analyses revealed that $Ba(Fe_{1-x}Sc_x)_{12}O_{19}$ has a cone-type helimagnetic structure with the base in the *ab* plane and the height along the *c* axis, whose proper screw in the *ab* plane propagates along the *c*-axis direction. These results suggest an antiferromagnetic superexchange interaction J_5, which is enhanced by the Sc substitution through shortening the bond distance Fe2-O1. Meanwhile, the superexchange interactions J_3 and J_4 are weakened through the preferred substitution of Sc^{3+} for the Fe4 site. This occurrence is supported by the results of the magnetic structure analyses that the angle α_{J5} between the magnetic moments coupled with J_5 increases from $0°$ and the angles α_{J3} and α_{J4} between the magnetic moments coupled with J_3 and J_4 decrease from $180°$ with increasing Sc concentration x. These facts cause the three competing superexchange interactions among J_3, J_4, and J_5. When these three superexchange interactions become comparable, the incommensurate helimagnetic structure of $Ba(Fe_{1-x}Sc_x)_{12}O_{19}$, in which three magnetic moments coupled with competing J_3, J_4, and J_5 point in different directions, is developed. Further enhancement of J_5 yields the spin-canted magnetic structure in the Sc-rich crystals. The correlation between the incommensurate helimagnetic structure and the superexchange interactions clarified in this paper will be useful for the design of magnetic oxide materials in the future.

[1] R. C. Pullar, Hexagonal ferrites: A review of the synthesis, properties and applications of hexaferrite ceramics, Prog. Mater. Sci. **57**, 1191 (2012).

[2] J. Smit and H. P. J. Wijn, *Ferrites* (Philips Technical Library, Eindhoven, 1959).

[3] P. B. Braun, The crystal structures of a new group of ferromagnetic compounds, Philips Res. Rep. **12**, 491 (1957).

[4] W. D. Towens, J. H. Fang, and A. J. Perrotta, The crystal structure and refinement of ferrimagnetic barium ferrite, $BaFe_{12}O_{19}$, Z. Krist. **125**, 437 (1967).

[5] See Supplemental Material at http://link.aps.org/supplemental/10.1103/PhysRevMaterials.7.014403 for the summary of crystal and magnetic structures of $BaFe_{12}O_{19}$, the refined parameter of each $Ba(Fe_{1-x}Sc_x)_{12}O_{19}$ sample, the comparison of the observed and calculated values of the crystal and magnetic structure factors, coordinate systems used for describing a magnetic moment, and determination process of the magnetic space groups. The Supplemental Material cites Refs. [21,29].

[6] E. W. Gorter, Saturation magnetization of some ferrimagnetic oxides with hexagonal crystal structures, Proc. IEE. **104**, 255 (1957).

[7] M. A. Darwish, V. A. Turchenko, A. T. Morchenko, V. G. Kostishyn, A. V. Timofeev, M. I. Sayyed, Z. Sun, S. V. Podgornaya, E. L. Trukhanova, E. Yu. Kaniukov *et al.*, Heterovalent substituted $BaFe_{12-x}Sn_xO_{19}$ ($0.1 \leqslant x \leqslant 1.2$) M-type hexaferrite: chemical composition, phase separation, magnetic properties and electrodynamics features, J. Alloys Compd. **896**, 163117 (2022).

[8] C. A. Herme, P. G. Bercoff, and S. E. Jacobo, Nd-Co substituted strontium hexaferrite powders with enhanced coercivity, Mater. Res. Bull. **47**, 3881 (2012).

[9] A. M. Balbashov, M. E. Voronchikhina, L. D. Iskhakova, V. Yu. Ivanov, and A. A. Mukhin, Single crystals growth of hexaferrits M-type $MTi_xCo_xFe_{12-2x}O19$ (M = Ba, Sr) by floating zone and investigation of their magnetic and magnetoelectric properties, Low Temp. Phys. **43**, 971 (2017).

[10] Y. Tokunaga, Y. Kaneko, D. Okuyama, S. Ishiwata, T. Arima, S. Wakimoto, K. Kakurai, Y. Taguchi, and Y. Tokura, Multiferroic M-type Hexaferrites with a Room Temperature Conical State and Magnetically Controllable Spin Helicity, Phys. Rev. Lett. **105**, 257201 (2010).

[11] S. Gupta, S. K. Upadhyay, V. Siruguri, V. G. Sathe, and E. V. Sampathkumaran, Observation of magnetoelastic and magnetoelectric coupling in Sc doped $BaFe_{12}O_{19}$ due to spin-glass-like phase, J. Phys. Condens. Matter. **31**, 295701 (2019).

[12] R. Tang, H. Zhou, W. You, and H. Yang, Room-temperature multiferroic and magnetocapacitance effects in M-type hexaferrite $BaFe_{10.2}Sc_{1.8}O_{19}$, Appl. Phys. Lett. **109**, 082903 (2016).

[13] Q. Zhu, R. Tang, H. Zhou, J. Zhang, J. Jiang, H. Yang, and X. Su, Chemical tuning of the magnetic properties of epitaxial $BaFe_{12-x}Sc_xO_{19}$ ($0 \leqslant x \leqslant 2.1$) hexaferrite thin films, J. Alloys Compd. **802**, 522 (2019).

[14] T. Kimura, G. Lawes, and P. Ramirez, Electric Polarization Rotation in a Hexaferrite with Long-Wave Magnetic Structures, Phys. Rev. Lett. **94**, 137201 (2005).

[15] S. Ishiwata, Y. Taguchi, H. Murakawa, Y. Onose, and Y. Tokura, Low-magnetic-field control of electric polarization vector in a helimagnet, Science **319**, 1643 (2008).

[16] H. Sagayama, K. Taniguchi, N. Abe, T. Arima, Y. Nishikawa, S. Yano, Y. Kousaka, J. Akimitsu, M. Matsuura, and K. Hirota, Two distinct ferroelectric phases in the multiferroic Y-type hexaferrite $Ba_2Mg_2Fe_{12}O_{22}$, Phys. Rev. B **80**, 180419(R) (2009).

[17] S. Ishiwata, D. Okuyama, K. Kakurai, M. Nishi, Y. Taguchi, and Y. Tokura, Neutron diffraction studies on the multiferroic conical magnet $Ba_2Mg_2Fe_{12}O_{22}$, Phys. Rev. B **81**, 174418 (2010).

[18] S. Hirose, K. Haruki, A. Ando, and T. Kimura, Mutual control of magnetization and electrical polarization by electric and magnetic fields at room temperature in Y-type $BaSr(Co_{2-x}Zn_x)Fe_{11}AlO_{22}$ ceramics, Appl. Phys. Lett. **104**, 022907 (2014).

[19] T. M. Perekalina and V. P. Cheparin, Ferrimagnetism of hexagonal ferrites, Sov. Phys. Solid State. **9**, 2524 (1968).

[20] O. P. Aleshko-Ozhevskii, R. A. Sizov, I. I. Yamzin, and V. A. Lubimtsev, Helicoidal antiphase spin ordering in hexagonal ferrites of the $BaSc_xFe_{12-x}O_{19}$ (M) system, Sov. Phys. JETP. **28**, 425 (1969).

[21] S. Utsumi, S. Tanaka, K. Maruyama, N. Hatakeyama, K. Itoh, J. Koike, A. Horikawa, H. Iriyama, H. Kanamaru, Y. Amako *et al.*, Flux growth and magnetic properties of helimagnetic hexagonal ferrite Ba(Fe$_{1-x}$Sc$_x$)$_{12}$O$_{19}$ single crystals, ACS Omega. **5**, 24890 (2020).

[22] K. Maruyama, S. Tanaka, S. Natori, I. Bizen, K. Amemiya, R. Kiyanagi, A. Nakao, K. Moriyama, Y. Ishikawa, Y. Amako *et al.*, Magnetic phase diagram of helimagnetic Ba(Fe$_{1-x}$Sc$_x$)$_{12}$O$_{19}$ ($0 \leqslant x \leqslant 0.2$) hexagonal ferrite, J. Alloys Compd. **892**, 162125 (2021).

[23] T. Ohhara, R. Kiyanagi, K. Oikawa, K. Kaneko, T. Kawasaki, I. Tamura, A. Nakao, T. Hanashima, K. Munakata, T. Moyoshi *et al.*, SENJU: A new time-of-flight single-crystal neutron diffractometer at J-PARC, J. Appl. Cryst. **49**, 120 (2016).

[24] T. Ohhara, K. Kusaka, T. Hosoya, K. Kurihara, K. Tomoyori, N. Niimura, I. Tanaka, J. Suzuki, T. Nakatani, T. Otomo *et al.*, Development of data processing software for a new TOF single crystal neutron diffractometer at J-PARC, Nucl. Instrum. Methods Phys. Res. A **600**, 195 (2009).

[25] V. Petříček, M. Dušek, M. Palatinus, and L. Palatinus, Crystallographic computing system JANA2006: General features, Z. Kristallogr. Cryst. Mater. **229**, 345 (2014).

[26] K. Momma and F. Izumi, VESTA 3 for three-dimensional visualization of crystal, volumetric and morphology data, J. Appl. Cryst. **44**, 1272 (2011).

[27] X. Dong, X. Zuo, Y. Wang, X. Cao, Y. Wang, and M. Feng, *Ab initio* study on exchange integrals and magnetic anisotropy change of BaFe$_{12-x}$Sc$_x$O$_{19}$ ($x = 0$, 0.5, 1, 1.5, 2), J. Magn. Magn. Mater. **513**, 167073 (2020).

[28] H. B. Cao, Z. Y. Zhao, M. Lee, E. S. Choi, M. A. McGuire, B. C. Sales, H. D. Zhou, J. -Q. Yan, and D. G. Mandrus, High pressure floating zone growth and structural properties of ferrimagnetic quantum paraelectric BaFe$_{12}$O$_{19}$, APL Mater. **3**, 062512 (2015).

[29] N. Qureshi, M. D. Ruiz-Martín, I. Puente-Orench, M. T. Fernández-Díaz, A. M. Balbashov, V. Yu. Ivanov, V. Skumryev, and A. A. Mukhin, Conical magnetic structures in multiferroic SrSc$_x$Fe$_{12-x}$O$_{19}$ hexaferrites derived from powder neutron diffraction, Phys. Rev. B **98**, 094411 (2018).

[30] S. V. Trukhanov, A. V. Trukhanov, V. A. Turchenko, V. G. Kostishyn, L. V. Panina, I. S. Kazakevich, and A. M. Balagurov, Structure and magnetic properties of BaFe$_{11.9}$In$_{0.1}$O$_{19}$ hexaferrite in a wide temperature range, J. Alloys Compd. **689**, 383 (2016).